Effect of Acoustic Radiation Force on the Distribution of Nanoparticles in Solid Tumors

Mercy Afadzi, Ola Finneng Myhre, Petros T. Yemane, Astrid Bjørkøy, Sverre H. Torp, Annemieke van Wamel, Sylvie Lelu, Bjørn Angelsen, Catharina de Lange Davies

***Abstract*—Acoustic radiation force (ARF) might improve the distribution of nanoparticles (NPs) in tumors. To study this, tumors growing subcutaneously in mice were exposed to focused ultrasound (FUS) either 15 min or 4 h after the injection of NPs, to investigate the effect of ARF on the transport of NPs across the vessel wall and through the extracellular matrix. Quantitative analysis of confocal microscopy images from frozen tumor sections was performed to estimate the displacement of NPs from blood vessels. Using the same experimental exposure parameters, ARF was simulated and compared to the experimental data. Enhanced interstitial transport of NPs in tumor tissues were observed when FUS (10 MHz, acoustic power 234 W/cm^2, 3.3 % duty cycle) was given either 15 min or 4 h after NP administration. According to acoustic simulations, the FUS generated an ARF per unit volume of 2.0 x 10^6 N/m^3. The displacement of NPs was larger when FUS was applied 4h after NP injection compared to after 15 min. This study shows that ARF might contribute to a modest improved distribution of NPs into the tumor interstitium.**

***Keywords* — acoustic radiation force; focused ultrasound; nanoparticle delivery; extravasation; interstitial displacement;**

I. Introduction

Although there has been considerable improvement in the treatment of cancer, effective treatments are still lacking for many types of cancers. Chemotherapy is often the treatment of choice for many advanced types of cancer; however, it is rarely curative for solid tumors [1] due to the lack of specificity towards the tumor cells. Encapsulating cytotoxic drugs in a particulate carrier such as liposomes, micelles or other nanoparticles (NPs) may reduce systemic drug toxicity to healthy tissues by delivering NPs selectively to tumor tissues [2-6]. The selective tumor accumulation is caused by the enhanced permeability and retention effect (EPR) [7]. However, physiological barriers in solid tumors [8] restrict the NPs from distributing homogenously throughout the tumor. Thus, due to the heterogeneous fenestration of blood vessels (BVs) in tumors and the poor penetration through the extracellular matrix (ECM), large areas of the tumor are not reached by the drug/NPs [9-11].

To overcome these challenges in drug delivery, development of new and effective treatments is highly needed for the drug to reach every tumor cell in sufficient quantities for complete eradication of the tumor. Various strategies including enzymatic degradation of the ECM [12], radioactive NPs [13], anti-angiogenic therapy causing normalization of BVs [14] have been proposed. In recent years focused ultrasound (FUS) has also shown promising results in preclinical [15-19] and clinical studies [20, 21]. Ultrasound (US)-mediated biological effects can be grouped into two categories, namely, thermal and non-thermal (mechanical) effects [18]. Thermal effects are associated with the absorption of acoustic energy by tissues, which results in heating. Non-thermal effects can be cavitation or acoustic radiation force (ARF). Cavitation is the formation and oscillation of microbubbles upon exposure to ultrasonic pressure waves. Stable volume oscillations of microbubbles cause microstreaming in the near vicinity of the microbubble. Increasing the power, these oscillations become more violent

This work was funded by the Central Norway Regional Health Authorities project no 4670000, and by The Research Council of Norway project number 240316.

M. Afadzi, P.T. Yemane, A. Bjørkøy, A. van Wamel, S. Lelu, and C.de L. Davies. are with Department of Physics, The Norwegian University of Science and Technology (NTNU), Høgskoleringen 5, 7491 Trondheim, Norway (email: Catharina.davies@ntnu.no) .

O. F. Myhre and B. Angelsen are with the Department of Circulation and Medical Imaging, The Norwegian University of Science and Technology (NTNU), P.O. Box 8905, 7491 Trondheim, Norway.

S. H. Torp is with the Department of Pathology, St. Olavs University Hospital, P.O. Box 3250 Sluppen, 7006 Trondheim, Norway, and Department of Clinical and Molecular Medicine, The Norwegian University of Science and Technology (NTNU), Einar Skjalgssons gt. 1, 7006 Trondheim, Norway.

and the microbubble will collapse producing microstreaming and jet streams in a process called inertial cavitation. Although cavitation is important and the most studied non-thermal US mechanism in the field of drug delivery, we believe that ARF could also be an important mechanism for local drug delivery.

When an US wave passes through a medium, there is an energy loss due to absorption and scattering of the wave. The energy loss corresponds to a loss of momentum in the wave, which is transferred to the medium. This generates a force on the medium in the direction of the net momentum vector of the wave. In a unidirectional collimated wave, the ARF is approximately aligned along the beam axis in the focal zone of the transducer. Depending on the magnitude of the ARF, tissue displacement can occur and the magnitude of the displacement is inversely proportional to tissue stiffness [22, 23]. When ARF acts on a fluid medium, it causes the formation of a flow, acoustic streaming [24], which may increase drug transport in the tissues. ARF has been reported to displace microbubbles circulating in the blood stream and push them towards the vessel wall. This might enhance receptor-ligand contact as well as induce shear forces, causing gaps in the endothelium of the vessel wall [25-28]. However, little attention has been given to the effect of ARF on the distribution of NPs in solid tumors. ARF might improve convection of the NPs from the blood vessel to ECM and enhance the penetration through the ECM and thereby improve the distribution of NPs throughout the tumor tissue.

This study aims to investigate the effect of ARF on the distribution of NPs (70 nm silica NP) in mice bearing subcutaneous human prostate cancer xenografts. The effect of ARF on the transport of NPs across the capillary wall and through tumor ECM were investigated by exposing the tumors to various US exposures given either 15 min or 4 h after intravenous injection of the NPs. These two-time points were chosen based on the circulation time of the NPs (half-life was measured to be approximately 2.3 h) to study the effect of FUS on extravasation (15 min) and intratumoral interstitial transport (4 h). High frequencies (5 MHz and 10 MHz) were applied as absorption and thus ARF are more likely to occur at higher frequencies. NP distribution in the tumor tissue was imaged in frozen tumor sections using confocal laser scanning microscopy (CLSM). The acquired tumor images were analyzed quantitatively to determine the amount of NP in the tumor tissue and the distance between the NP location and the nearest BV wall. The enhanced NP concentration in the tumor and improved distribution of NPs in the ECM can be due to ARF, cavitation and thermal effects. To demonstrate that the high frequency and highly focused US exposure applied can induce ARF, the ARF obtained by the US parameters used in the experimental work was simulated, and the simulations were compared to the experimental data. The experimental data supported that FUS displaced NPs in tumor ECM. ARF can partly push NPs directly, but more likely ARF generates acoustic streaming which causes the displacement of NPs.

II. MATERIALS AND METHODS

A. *US exposure set-up and protocol*

Two circular single element US transducers were selected for the experiments based on initial simulations of ARF. The transducers were selected from the Olympus high-power Immersion series and have center frequencies of 5 and 10 MHz.

A schematic representation of the US exposure set-ups used in the experiment can be found in Fig. 1. Each transducer was fixed to a 3D positioning stage controlled by in-house software programmed in LabView. To position the transducers correctly relative to the tumor, pulse-echo measurements were performed with a 5900PR pulse-receiver (Panametrics, USA) before treating each animal. The therapeutic pulses were generated using an arbitrary waveform generator (AWFG, 33522A, Agilent Technologies, USA) connected to a 2100L amplifier (ENI).

The US setup consisted of two custom-built parts (Fig. 1); a PVC base (not shown) with an acoustically absorbing mat (10 mm thick, Aptflex F28, Precision Acoustics, UK) where the animals were placed, and a PVC cone (200 mm top diameter), which was filled with degassed water into which the transducer was partially submerged. The bottom of the cone has a circular 2 mm diameter aperture, which is covered by an optically and acoustically transparent Mylar film (23 µm thick) (not shown). The base and the cone are connected by screws so that their relative positions can be adjusted. The animals were placed on an acoustically absorbing mat so that the hind leg of the animal could be acoustically coupled with the absorbing mat. This was done to avoid multiple scatterings of the US beam, which could cause ARF in directions other than along the beam axis. Acoustic coupling gel was subsequently applied using a syringe between the tumor and the Mylar film to ensure good acoustic coupling. For the 5 MHz experiments, the water cone is replaced with a water filled plastic bag that was placed on top of the tumor.

The nominal beam widths (-3dB) of the two transducers are 0.61 mm (5 MHz) and 0.34 mm (10 MHz). To treat a larger area of the tumor, a step motor was used to move the transducers in 3 x 3 positions as shown in Fig. 1B, covering respectively 1.02 mm x 1.02 mm and 1.8 mm x 1.8 mm of the tumor in xy-direction, using respectively the 10 MHz and 5 MHz transducer. In the z-direction along the US beam, the whole tumor was exposed to US. Each position was exposed for 400 s for a total scanning time of 1 h. The voltages into the 10 MHz and 5 MHz transducers were 210 Vpp and 160 Vpp, respectively. The input power was estimated by measuring the voltage on the transducers and their electrical input impedance. US parameters (acoustic pressure and duty cycle) resulting in less than 6.1 W were applied which was the maximum effect to be used to avoid heating and damage of the transducer, according to the manufacturer.

B. *Characterization of US transducers*

Characterization of each transducer was done in accordance with international measurement standards [29]. A water tank measurement system (Onda AIMS-III) was used, and the pressure was recorded with a HGL-0085 hydrophone (Onda Corporation, USA) using an AH-2020 pre-amplifier (Onda Corporation, USA).

The output power from each transducer was estimated from far-field pressure measurements, using low excitation voltage (11 Vpp for the 10 MHz and 15 Vpp for the 5 MHz) to minimize the effect of non-linear propagation in water. These measurements were combined with low voltage and high voltage (210 Vpp for the 10 MHz and 160 Vpp for the 5 MHz) near-field pressure measurements 1 mm from the transducer surfaces to estimate the surface pressure generated by the high voltage excitation. Further details can be found in Appendix A.

The estimated transducer surface pressure was used as an input parameter in simulations of the ARF generated by each transducer. The parameters used in the experiments and simulations are given in Table I.

C. *Investigation of thermal effect*

To investigate whether the US exposure causes any thermal effect, ex-vivo chicken breast was exposed to the US exposures parameters used in the experiment. All measurements were done at 37 ºC using a Fiber-optic hydrophone system (Fiber-optic hydrophone system, Precision acoustics Ltd, UK). The sensor of the hydrophone was inserted between two slices of the tissue positioned at the focus of the probe and the pressure wave was monitored on an oscilloscope. The temperature reading started 60 s before the US exposure, which lasted for 400 s and the temperature reading was stopped after 560 s.

D. *Simulation of ARF*

The ARF is given by the transfer of momentum from the wave to the medium, and is proportional to the average intensity of the wave and the attenuation of the medium [30]. To account for the frequency dependence of the attenuation in the medium, the ARF per unit volume (ΔV) can be expressed as (see Appendix B);

$$\frac{\Delta F_r(r,\omega)}{\Delta V} = \frac{1}{2\pi T_p \rho c^2} \int \sigma_e(r,\omega) |P(r,\omega)|^2 \, d\omega \quad (1)$$

where σ_e (r, ω) is the attenuation cross section per unit volume, ρ density, c speed of sound, P (r, ω) is the temporal Fourier transform of the pressure at the point r, and T_p is the pulse duration. ω is angular frequency (ω =2πf), where f is frequency.

Acoustic attenuation in biological tissue follows a power law frequency dependence:

$$\sigma_e(r,f) = \alpha_0(r) f^{b(r)} \quad (2)$$

where α_0 is attenuation constant, f is the frequency in MHz, and b is the frequency-power law exponent. b is typically in the range of $1 \leq b \leq 1.6$ in most biological tissues and 2 in water [31].

A nonlinear wave propagation in a medium introduces higher order of harmonics which depend on the initial pressure of the wave, the acoustic absorption (σ_e) of the medium, the nonlinearity parameter (B/A) of the medium, and the propagation distance through the medium. As shown in Eq (2), the harmonics are more strongly attenuated by the medium than the fundamental, and therefore contribute significantly to the ARF. To calculate the ARF in an irradiated medium using (1), the pressure P(r, ω) and the absorption (σ_e(r, ω)), were first calculated using a simulation software, which is based on the Westervelt equation and uses the same numerical solver as ABERSIM [32].

In the simulations of ARF, water was used as the propagation medium for the first 55 mm and 45 mm from the transducer surface for the 5 and 10 MHz transducers, respectively. Uniform tissue was used for the remaining distances. The parameters α_0 = 0.00220 dB/(cm MHz) [31], b = 2, c = 1482.3 m/s, density ρ = 1000 kg/m^3, and B/A = 4.96 [33] were used for the simulation of the propagation in water. Although the experimental work was conducted in prostate adenocarcinoma, parameters for human prostate tissue were used in the simulations. The value b=1.3 (median of the range 1-1.6) was chosen due to lack of experimental data. The acoustic attenuation in prostate has been measured as σ_e=3.9 dB/cm at 5 MHz [34]. With b=1.3 and f=5 MHz, (2) yields α_0=0.48 dB/(cm MHz$^{1.3}$), which was used in the simulations. The other parameters were c = 1561 m/s [34], ρ = 1045 kg/m^3 [35] and B/A = 7.43 (B/A of muscle [33]).

E. *Displacement of NPs due to the direct effect on the NPs and streaming*

The extinction of the US wave produces an ARF on the NP and the fluid in which the NP is submerged. US extinction occurs on a spatial scale that is comparable to the wavelength of the US wave. NPs are 2-3 orders of magnitude smaller than the wavelength, and the change in wave momentum over the particles is therefore small. The direct effect of ARF on NP displacement can be estimated by the Stoke's drag equation. Assuming that the Reynolds number is very small[36], the terminal translational velocity of the NPs can be substituted in the Stokes drag equation [37-39]. Under the influence of ARF, the maximum velocity, u_p, of the NPs is estimated from:

$$\frac{\Delta F_r}{\Delta V} V_p = 6\pi\eta R_p u_p \quad (3)$$

where η is the dynamic viscosity of the fluid, R_p is the radius of the NP, and V_p is volume of the NP. The displacement was calculated from:

$$\psi_p = \frac{\Delta F_r}{\Delta V} \frac{V_p T_{on}}{6\pi\eta R_p} = \frac{2R_p^2}{9\eta} \frac{\Delta F_r}{\Delta V} T_{\text{on}} \quad (4)$$

where T_{on} is the total time the particle was exposed to the ARF. For a pulsed excitation, $T_{on}=T_{tot}\cdot DC/100$, DC is the duty cycle in percentage, $DC=T_p\cdot PRF\cdot 100$ and T_{tot} is the total scanning time for a given location. The pulse repetition frequency (PRF) is also defined as $1/T_R$ where T_R is the pulse repetition period. The fluid surrounding the NP will also be set in motion by the attenuation of the passing wave; a phenomenon known as acoustic streaming. This motion may transport the NPs through the interstitium if the NPs can move freely with the fluid, i.e. if the cross section of the interstitial space is larger than the particle size. By modelling the interstitium as a porous medium [40] the velocity of the fluid can be calculated by Darcy's law:

$$U(r) = K'\nabla P \quad (5)$$

where U is the fluid velocity, K’ is the hydraulic conductivity of the interstitium [22] and ∇P is the pressure gradient on the medium that is the driving force for the fluid. Assuming ARF is the only unbalanced force acting on the medium, ∇P = ΔFr/ΔV. NPs can be moved in the flow caused by acoustic streaming and if the velocity of the NPs and the flow is the same, the displacement of the NPs can be estimated as:

$$\psi_{ps} = UT_{on} = K'\frac{\Delta F_r}{\Delta V}T_{on} \qquad (6)$$

F. Cells and animals

Human prostate adenocarcinoma cells (PC3, American Type Culture Collection, USA) were grown in Dulbecco’s Modified Eagle Medium (Life Technologies AS, Norway) supplemented with 10% fetal bovine serum (Sigma-Aldrich, Norway). The cells were grown at 37 °C and in 5% CO_2.

Female Balb/c nude mice (C.Cg/AnNTac-Foxn1nu NE9, Taconic, Denmark) were purchased at 6 – 8 weeks of age. The animals were housed in IVC cages (model 1284L, Techniplast, France) in groups of 5 under conditions free of specific pathogens according to the Federation of European Laboratory Animal Science Association’s [41] recommendations. Thus, they had free access to food and sterile water and the environment was controlled with temperatures kept between 19 – 22 °C and a relative humidity between 50 – 60%. All experimental procedures with animals were conducted following the protocols approved by the Norwegian National Animal Research Authorities, i.e., the Norwegian Food Safety Authority. Before implanting the cells, the mice were anaesthetized with isoflurane and 3 $\times 10^6$ PC3 cells in suspension (50 µl) were then subcutaneously injected on the lateral aspect of one hind leg. The tumors were allowed to grow for 3 – 4 weeks until the diameter of the tumor was between 7–10 mm. PC3 tumors were used as we previously have characterized and used the tumor model in studies combining US and microbubbles [15, 47].

G. Measurements of the circulation half-life of NPs

PEgylated Silica NPs (SiFluor 560, Active Motif, USA) with a diameter of 70 nm containing chromeo^{TM} dyes were used, as these NPs represent the size of commonly used NPs and they are stable and non-degradable, highly fluorescently labeled with a dye not leaking out of the NPs thereby enabling tracking of the NPs.

Mice (n = 4) were anesthetized with ~ 0.2 ml a solution of Ketamin/Xylazin/saline at a ratio of 1: 0.25: 3.75. The temperature of the mice were monitored and kept at 35° C. After intravenously injection of 200 µl (2 mg/ml) of the NPs, blood samples of approximately 20 µl were drawn from the saphenous vein into an Eppendorf tube containing 40 µl of 10 IU/ml heparin at pre-injection and 10 min, 30 min, 1, 2, 4, 6 and 24 h post-injection. The tubes were weighed before and after blood sampling and then centrifuged (IEC Micromax, Tamro Med Lab ASA, Norway) at 3000 rpm for 7 min before collecting 20 µl of the plasma (the supernatant) for fluorescent measurement. The fluorescence intensity was measured using a Tecan Infinite 200 Pro microplate reader (Tecan group Ltd, Switzerland). The chromeo dye labelled NPs were excited at 555 ± 9 nm, and the fluorescent signal recorded at 585 ± 20 nm.

H. US exposure after intravenous injection of NPs

Mice bearing subcutaneous prostate cancer xenografts were anesthetized with a solution of Ketamin/Xylazin/saline as described above. PEGylated silica NPs (70 nm in diameter) were injected intravenously (200 µl and 2 mg/ml) through the tail vein. To investigate the effect of ARF on the extravasation of NPs across the capillaries, tumors were exposed to 10 MHz US 15 min after injection of NPs (n=3 mice). The effect of ARF on the transport of NPs through the ECM was investigated by exposing the tumors to 10 MHz (n=5 mice) and 5 MHz (n=2 mice) US 4 h after NP injection. At this time point very little NPS are circulating, and some NPs should have extravasated by the EPR effect. The unexposed animals (control group) were handled in the same way as the other animals, with the exception of US. Thus, the control mice were sacrificed after 15 min+1 h (1 h US exposure) (n=2 mice) and after 5 h (n=2 mice). To increase the number of tumors in the control groups, sections from unexposed tumor areas were added to the controls. This gives n = 6 for 15 min control and n = 9 for 4 h control.

I. Preparation and imaging of tumor sections

Immediately after US exposure, 100 µl (1 mg/ml) of FITC-lectin (fluorescein-labeled Lycopersicon esculentum (Tomato) lectin; Vector Laboratories, USA) diluted in 0.9% NaCl was intravenously injected and allowed to circulate for 5 min to stain the functional BVs. Then, the mice were euthanized by cervical dislocation, and the tumors were excised, embedded in OTC Tissue Tec (Sakura Finetek Europe, Netherlands) and frozen in liquid N_2. Before sectioning the tumor, 500 µm was removed from the edge to remove any normal tissues. Subsequently, the tumor was sectioned into 25 µm thick frozen sections (S), and after every third section, 200 µm of the tumor was removed (Fig. 2). This was repeated 6 or 8 mm into the tumor (depending on the tumor size). Considering the beam widths of the transducers used, the treated area corresponded to approximately 2 – 4 (10 MHz group) and 4 – 7 (5 MHz group) positions (P). The US exposed positions were identified as explained in “III.E. Identifying the US-treated areas in tumors”. The sections were mounted on objective glass slides with Vectashield mounting medium (Vector Laboratories, USA) and sealed with a glass cover slip and nail polish.

J. Confocal laser scanning microscopy

The tumor tissue sections were imaged using a Leica SP5 CLSM (Leica Microsystems, Germany) equipped with a 20X air objective (NA = 0.7). Both bright field and fluorescence (FL) 8 bit micrographs were recorded. The FITC-lectin and the chrome dye labelled NPs were sequentially excited at 488 and 561 nm, respectively. The fluorescence of the two dyes, FLFITC and FLnp, was detected in the range of 500 – 570 nm and 575 – 649 nm, respectively. The laser intensities and detector settings were kept constant for all of the images acquired. The pinhole was set to 2.8 AU to increase the signal-to-noise ratio and optical slice, and z-stacks were recorded using scan zoom 4 and line average 4. The voxel size was 0.38 × 0.38 × 0.79 µm^3 and corresponded to an image size of 194 × 194 µm^2 in the xy-plane.

K. Post-processing of CLSM images

The image processing program ImageJ (version 1.5) was used to pre-process and manually threshold the z-stacks. The optimal threshold values for the FLFITC and the FLnp images were determined to be 18 and 20, respectively, after examining several sections. The median filter in the 3D Fast Filters plugin was applied for noise reduction (kernel dimension 0.76 × 0.76 × 0.79 μm^3). To ensure that all pixels in a BV connect, the 3D Fill Holes plugin was applied to the binary FLFITC stacks. To quantify the NPs in the FLnp stack and their distance to the nearest BV in the corresponding FLFITC stack, a custom-designed MATLAB script was used. Traces of BVs volumes smaller than 10 μm^3 were deleted from the FLFITC stack to ensure that only objects not considered to be a vessel were removed. For each pair of z-stacks, the total volume of NP pixels outside the vessels were estimated. The minimum distance from the NP to the border of the nearest BV was computed. The BVs in tumors have a chaotic morphology, and it is not possible to know which BV the NPs have left. The distribution of NPs decreased with distance from BV. In some cases, a small peak was seen beyond 120 µm, and interpreted as NPs from BVs in another plane or not stained BVs. Thus, only NP up to 120 µm were included. The data was imported into SigmaPlot (version 14.0) for statistical analysis.

L. Histology

To determine whether the US exposure caused any tissue damage, 25-µm frozen sections from the treated area in the exposed tumors and unexposed tumors were stained for histology using hematoxylin-eosin-saffron (HES). The sections were then dehydrated and mounted using a xylene based medium and a cover slip. The sections were analyzed with a Nikon Eclipse 80i microscope equipped with a 20 X air objective by an experienced pathologist, scoring for micro-bleeding and damaged cells.

M. Statistical analysis

To test for significant difference across groups, a non-parametric test (Kruskal-Wallis) was conducted. Mann–Whitney and Dunn tests were used for pairwise comparison within and across groups, respectively. A p-value below 0.05 was considered statistically significant.

III. RESULTS

A. Characterization of the US transducers

The estimated surface pressures were 206 kPa (10 MHz, 210 Vpp), and 133 kPa (5 MHz, 160 Vpp). These pressures were used as input parameters when simulating the ARF.

B. Simulation of ARF and estimation of NP displacement

Axial peak positive and negative pressures and axial ARF as a function of depth (normalized to the focus of each transducer) for power law exponent $b = 1.3$ are shown for both transducers (Fig. 3). Since b is typically in the range of $1 \leq b \leq 1.6$ in most biological tissues, the median b value was chosen for the simulation in tissue. The ARFs at the transducer foci were 0.7 x 10^6 N/m^3 and 2.0 x 10^6 N/m^3 for the 5 MHz and10 MHz transducer, respectively (Fig. 3B, Table I).

The displacements of NPs in the ECM caused by the direct effect of ARF and acoustic streaming are shown in Table II. The displacements depend on tissue characteristics such as viscosity and hydraulic conductivity which varies considerably between tissues, thus a range of displacements are presented. The viscosities of 3.2 mPa·s in the blood plasma [22] and 265-3500 mPa·s in the tumor ECM [42, 43] were used. The estimated displacements caused by the simulated ARF using (4) were almost negligible being mainly in the nm range. Using a range of published values for hydraulic conductivity ($1x10^{-8}$ cm^2 mmHg^{-1} s^{-1} and $1000x10^{-8}$ cm^2 mmHg^{-1} s^{-1}) [44] together with the simulated ARF and Eq (6), the effect of acoustic streaming on the displacement of NPs was estimated and found to be much larger than the direct effect on the NPs (Table II). The longest displacement was 200 µm using 10 MHz at pulse intensity of 234 W/ cm^2 and duty cycle of 3.3%. Comparing the longest displacements estimated by acoustic streaming and by direct effect of ARF, the displacements due to acoustic streaming were found to be approximately 50 to 270 times higher than the direct effect.

ARF might direct the circulating NPs towards the blood vessel wall. Assuming that the viscosity in blood plasma is 3.2 mPa·s [45], the displacement of NPs in blood was found to be respectively, 2.3 µm (10 MHz) or 0.25 µm (5 MHz) (Table II).

C. Circulation half-life of NPs

The circulation half-life of the silica NPs was found by measuring the fluorescence of the NPs in blood at different time points after NP injection. The ratio of NP fluorescent intensity (FL) and the volume of blood (VB) was plotted as a function of post-injection time (Fig. 4). A bi-exponential decay function was fitted to the experimental data, and the circulation half-life of the NPs in blood was found to be approximately 2.3 h.

D. Temperature measurements

US exposure using the 5 and 10 MHz transducer increased the temperature in the ex-vivo chicken breast by 0.80 ±0.14°C (Fig. 5 A) and 8.81±1.07ºC (Fig. 5 B). Rapid temperature fluctuations were seen for the 10 MHz exposure which could be due to cavitation activity on the tip of the sensor which also has been suggested by others [46], although the probability for cavitation at this MI is not high. If bubbles are present between the sensor and transducer, it leads to a temporary reduction in temperature while a temporary increase occurs if bubbles are on the back of the sensor,

E. Identifying the US-treated area in tumors

Only a small part of the tumor was exposed to US, and to identify the treated tumor section, frozen sections at 9 –15 positions distributed throughout the tumors were imaged by CLSM and analyzed by ImageJ and a customized Matlab script. Representative CLSM images are shown in Fig. 6.

The maximum distance travelled by NPs from the nearest BV was determined for the sections from untreated and treated tumors (Fig. 7). In control tumors 10-12 positions were analyzed in 4 tumors to investigate the variations in the untreated control and a random variation in maximum distance travelled was found (Fig. 7 A). In most of the treated tumors, sections from 4-7 neighboring positions showed NPs with larger displacement from the BV (Fig. 7 B), and 4-7 neighbor positions corresponded to the size of the tumor in x-direction that was exposed to the maximum US intensity (-3 dB, 1.02 mm and 1.8 mm for 10 MHz and 5 MHz, respectively). Thus, based on this systematic increase in NP displacement, this tumor area was assumed to be exposed to US. However, it should be emphasized, that although treated tumor sections were identified, the exact exposed area along the section (y-axis) was not known.

F. Extravasation of NP across the capillary wall

The uptake of NPs was estimated from the volume of the NPs outside the BVs and the median volume per stack is presented in box plots (Fig. 8). Only, US exposure at 5 MHz 4 h after administration of NPs enhanced the median NP volume. Median NP volume was significantly improved when tumors were exposed to 10 MHz US 15 min after NP administration compared to tumors treated with 10 MHz 4 h after NP administration.

G. Displacement of NPs from blood vessels into the ECM

To quantify the penetration of NPs into the ECM, the median displacements of NPs from BVs were estimated. Box plots with the median (solid line) measurements are shown in Fig. 9a. Most of the NPs will be located close to the BV. Thus, we also estimated how far the 10% of NPs being displaced mostly, had moved (Fig 9b). These data indicate that 10 MHz given 4 h after NP injection is more efficient than the other treatment groups. The median distance and the top 10% distances travelled from the BV were significantly increased compared with the other groups (Fig. 9b). For US given 4 h after NP injection, the median of the NP displacements and the top 10% distance travelled were 14.7 µm and 96.1 µm respectively, for 10 MHz at 3.3% duty cycle, and 11.3 µm and 57.7 µm, respectively, for 5 MHz at 0.6% duty cycle.

H. Histology

To investigate whether US exposure caused any tissue damage, frozen sections from treated and unexposed tumors were stained for histological (HES) analysis. The sections were analyzed by an experienced pathologist. No pathological damage was detected in the treated and unexposed sections. No necrosis, hemorrhage, edema, inflammation or changes in BVs were observed (Fig. 10). Furthermore, there was no significant difference detected in the volume of BV in the exposed and unexposed groups (data not shown).

The histology sections confirmed that PC3 tumors have a high vascular density in the tumor periphery and a necrotic central core and a relative high content of collagen throughout the tumor [47].

IV. DISCUSSIONS

ARF is one of the three US related mechanisms, next to cavitation and hyperthermia, which can induce a biological effect in tissues. In this study, 5 MHz and 10 MHz FUS was applied to generate ARF in subcutaneous prostate tumors in mice. FUS was given 15 min or 4 h after intravenous injection of 70 nm silica NPs to study respectively the effect on extravasation and penetration in the ECM. The effect of FUS on the transport of the NPs across the BV wall and through the ECM of the tumors was investigated by performing a quantitative analysis of the CLSM images taken from the tumor tissue sections. Using the same exposure parameters, the ARF was calculated based on nonlinear acoustic simulations and bulk material parameters. The simulations were compared to the experimental data. It should be emphasized that the computational model implemented in the study is simplified compared to the in vivo conditions. Furthermore, as highly focused US transducers were used to increase the likelihood to achieve ARF, only a small part of the tumor was exposed to US, and identifying these exposed regions was challenging. Thus, the results presented are probably an underestimation of the ARF effect as tumors areas not exposed to ARF are included in the analysis.

A. ARF enhances extravasation of NPs

The fraction of NPs outside BVs was estimated, and only US exposure at 5MHz give 4 h after NP administration was found to increase the extravasation of NPs compared to untreated controls. US exposure given 15 min after NPs administration was more effective in improving the transport of NPs across the BVs than when exposing tumors to US 4 h after NPs administration. This is in accordance with the circulation half-life of the NP, which was approximately 2.3 h; thus, very few NPs are circulating 4 h after NP administration.

Thus, ARF don't seem to have a major effect on extravasation. Any effect might be due to both ARF pushing NPs toward the vessel wall and across the vessel wall. ARF is reported to displace microbubbles, cells and NPs circulating in the blood towards the vessel wall [26, 27, 48-52]. Furthermore, in a fluid medium, ARF can produce a steady flow, i.e., acoustic streaming [24], which may increase the transport of NPs between the endothelial cells and across the vessel wall. Previous studies have shown that high frequency US can improve extravasation of NPs from BVs into the interstitium [54-56].

Even though fenestrations in the tumor BVs support NP extravasation, it also leads to a high interstitial fluid pressure (IFP), which limits transvascular transport of NPs. The IFP in tumors has been reported to be on the order of 10 – 30 mmHg [53]. Interesting, the magnitude of the ARF per unit volume generated in our study was found to be (0.7 - 2.0) x 10^6 N/m^3 which corresponds to 5 - 15 mmHg/mm; i.e. in the same order as IFP in general.

B. ARF enhanced displacement of NPs from blood vessels into the ECM

A successful therapeutic response of drug-loaded NPs requires that the NPs are distributed evenly throughout the interstitium after extravasation to kill all tumor cells. The distribution of NP in the tumors is impeded by the composition and structure of the tumor ECM [57-59] and the high IFP [53, 60]. FUS was found to increase the median of the top 10% displacements of NPs from BVs by 1.5-fold compared to the untreated tumors., Furthermore, allowing NPs to circulate for 4 h before treating the tumors with US was more effective in improving the penetration of NPs further away from the vessels than applying US 15 min after NP administration. This is probably due to the EPR-effect, which caused a larger number of NPs in the ECM 4 h after the NP injection at the time of FUS exposure. The improved penetration of NPs in the ECM might be due to ARF-induced acoustic streaming [61, 62], rather than pushing the NPs directly as the NPs have a diameter less than the US wavelength. Accordingly, the estimations of displacements of NPs due to ARF showed that acoustic streaming was much more effective than directly pushing the NPs. Both experimental results and simulations showed that 10 MHz induced a larger displacement of NPs than the 5 MHz exposure. The experimental median displacements were in both cases within the range of the simulated displacements. The top 10% displacements after 10 MHz exposure was in the upper range of the simulated values, whereas for the 5 MHz exposure the experimental displacement was larger than the simulated. This discrepancy might be due to not using correct values for the hydraulic conductivity of the prostate tumor tissue, or that the NP might arise from a not labelled BV or a BV outside the imaged plane.

The extent of tissue displacement induced by ARF has be shown to depend on acoustic intensity (I_{SATA}) and the duration of US [63]. Hence, the 10 MHz probe might have induced larger tissue displacement than the 5 MHz due the fact that the average acoustic intensity and the total exposure time were higher for the 10 MHz than for the 5 MHz.

The improved distribution of NP in the ECM could be a result of US-enhanced permeability of the ECM. ARF and pulsed high-intensity FUS (1 MHz) have been reported to increase the gap size between muscle fibers leading to an increased tissue permeability[54, 56]. An increase in tissue permeability may also result in increased hydraulic conductivity and acoustic streaming, which may increase NP transport.

The overall aim of this study was to study whether it is possible to improve NP distribution in tumor tissue using ARF. Our data seems to suggest that ARF can improve both extravasation and penetration through ECM. However, as unexposed areas of the tumor also are included in the CLSM images, the results are an underestimation the US effects. Moreover, we cannot exclude that the observed effects are partly due to increase in the temperature and generation of microbubbles causing cavitation. A temperature increase was found in ex vivo tissue when applying the 10 MHz exposure, thus hyperthermic effect and effect caused by ARF cannot be separated. However, applying 5 MHz increased the temperature less than 1 °C and US exposure caused a displacement of NPs away from the BV. Thus, we do not believe that the improved extravasation or penetration in the ECM is mainly a temperature effect, although the increase in temperature can partly be responsible. The temperature increase in the tumor is probably lower than in ex vivo chicken breast due to the blood flow removing heat [64, 65]. Increasing the temperature might enhance the vascular permeability, blood flow and diffusion of NPs, but a temperature increase of 9 °C will according to Stoke-Einstein's equation (assuming diffusion in solution) enhance the diffusion coefficient only approximately 3%. It has also been reported that exposure for more than an hour is needed to obtain thermal effects [66].

The main parameter describing cavitation in tissue is the mechanical index of the pulse which is given by:

$$MI = \frac{-P}{\sqrt{f}} \tag{7}$$

where P is the negative peak pressure in MPa and f is the center frequency of the pulse in MHz. In diagnostic imaging, the MI should be less than 1.9. The 10 MHz exposure which produced largest NP displacement generated a MI of 1.0, whereas the 5 MHz which showed less NP displacement had the highest MI of 1.4. This indicates that cavitation alone cannot explain the observed displacement of the NPs from BV, although it cannot be ruled out that cavitation plays a role for the 5 MHz exposure.

C. *No tissue damage*

Histological analysis of tumor sections did not show any tissue or vessel damage caused by the US. Furthermore, no mice showed any symptoms of problems during or after FUS treatment. Thus, the applied FUS is considered safe. This is consistent with other studies using even higher acoustic powers compared to our study where no permanent damage in muscle or tumor tissues was observed [54, 56, 67]. The safety of US imaging has been extensively studied both for short term and long term effects, and MI less than 1.9 is considered safe, whereas for contrast-enhanced US imaging the MI should be less [68]. The MI used in the present study adding no microbubbles, is thus within the international safety recommendations.

D. *Clinical impact*

The magnitude of the observed FUS-induced effects are similar to the effect of cavitation we reported using the same tumor model and NPs forming a shell around gas bubbles [55]. Both ARF and cavitation increased the tumor uptake up to 2-3 times and the NPs displacement was up to 1.5 times compared to untreated control tumors. In another study we found that cavitation increasing the NPs uptake 2.5 times, was sufficient to eradicate all tumors in mice treated two times with FUS, and drug loaded NP forming a shell around the microbubbles [69]. This indicates that a rather modest improvement in tumor uptake and distribution of NPs might be of clinical importance. However, studies of the therapeutic effect of drug loaded NPs combined with ARF also when using lower and more clinically relevant frequencies are needed to verify that ARF can have a clinical impact.

V. CONCLUSION

The present study shows that ARF per unit volume of 2.0 x 10^6 N/m^3 generated by 10 MHz US, power 9.6 W/cm^2 and 3.3% duty cycle is capable of improving the transport of a small fraction of NPs in tumor ECM when US is given both 15 min or 4 h after NP administration, 4 h administration of NPs being the most effective. An US-induced displacement was found both experimentally and by simulations. The simulations showed that acoustic streaming is the dominant effect of ARF on the NPs.

APPENDIX

A. Appendix A: Surface pressure

The generated surface pressure on a transducer at high voltage, p_S^{HV}, is hard to measure directly due to the interference in the near-field, and it is hard to estimate accurately from far-field pressure measurements due to non-linear distortion. The surface pressure is therefore estimated using a combination of near-field (NF) and far-field (FF) measurements.

The far-field pressure at low voltage, p_{LF}^{FF}, is measured with a hydrophone in a uniformly sampled grid perpendicular to the beam axis, at a depth z_1. The grid resolutions are Δx and Δy, and i,j specify the hydrophone position index. The number of measurement points in each dimension is I+1 and J+1. Letting T_p denote the duration of the ultrasound pulse, and Z denote the characteristic impedance of water, the measured acoustic power at low voltage is

$$\mathrm{P_{LV}} \approx \mathrm{\Delta x \Delta y} \sum_{\mathrm{i}=-\mathrm{I}/2}^{\mathrm{I}/2} \sum_{\mathrm{j}=-\mathrm{J}/2}^{\mathrm{J}/2} \frac{1}{\mathrm{ZT_p}} \int_0^{\mathrm{T_p}} \left|\mathrm{p_{LV}^{FF}}(\mathrm{i\Delta x, j\Delta y, z_1, t})\right|^2 \mathrm{dt} \qquad \text{(A.1)}$$

The measurement is taken at low voltage to avoid non-linear distortion of the pulse.

In the near-field, $z=z_0$, the pulse distortion is negligible irrespective of the input voltage. When the absorption in water is neglected, the output power at high voltage, P_{HV}, is found by scaling P_{LV} using the ratio of measured near-field pressures at low voltage, p_{NF}^{LV}, and high voltage, p_{NF}^{HV};

$$P_{\mathrm{HV}} = \left(\frac{p_{\mathrm{NF}}^{\mathrm{HV}}}{p_{\mathrm{NF}}^{\mathrm{LV}}}\right)^2 P_{\mathrm{LV}} \qquad \text{(A.2)}$$

The surface pressure amplitude at high voltage, p_S^{HV}, is found by using the plane wave relation [27] to substitute P_{HV} in (A.2). For a circular transducer with a diameter D, the power at the surface is $P_{HV}=\pi D^2 (p_S^{HV})^2/8Z$, which combines with (A.2) to yield

$$p_{\mathrm{S}}^{\mathrm{HV}} = \frac{p_{\mathrm{NF}}^{\mathrm{HV}}}{p_{\mathrm{NF}}^{\mathrm{LV}}} \frac{2}{D} \sqrt{\frac{2ZP_{\mathrm{LV}}}{\pi}} \qquad \text{(A.3)}$$

The surface pressures in Section IIA were calculated using the nominal transducer diameters for each transducer (seeTable I). The rest of the measurement parameters are shown in Table II.

B. Appendix B: Acoustic Radiation Force (ARF)

The radiation force on an arbitrary volume, ΔV, is, by Newton's law, given by the transferal of momentum from a passing wave to the volume. Let u(r,t) be the vibration velocity vector field at the position r, and ρ be the density of the volume ΔV. The radiation force on the volume is given by

$$\begin{aligned} F_r(r) = -\int_V \rho \frac{1}{T} \int_0^T & (u(r,t)\nabla u(r,t) \\ & + (u(r,t)\nabla) u(r,t)))\, \mathrm{d}t\, \mathrm{d}V \end{aligned} \qquad \text{(B.1)}$$

where the time T is the duration of the passing wave. Assuming that the passing wave can be approximated as a plane wave travelling in the positive z direction, the vibration velocity vector field is $u(r,t)=u(r,t)\ e_z$ where e_z is the unit normal along the z-axis. The integrand of (B.1) simplifies to

$$\begin{aligned} & u(r,t)\nabla u(r,t) + (u(r,t)\nabla) u(r,t)) \\ & \qquad = 2u(r,t)\, \frac{\mathrm{d}u(r,t)}{\mathrm{d}z} e_z \end{aligned} \qquad \text{(B.2)}$$

For a plane, progressive wave, the pressure is related to the vibration velocity by the characteristic impedance, Z=ρc, so that p(r,t)=ρc u(r,t), where c is the speed of sound. It is also known that the absorption of a plane progressive wave is

$$\begin{aligned} \frac{dI(r,\omega)}{dz} = -\sigma(r,\omega) I(r,\omega) \rightarrow \frac{dP(r,\omega)}{dz} \\ = -\frac{1}{2}\sigma(r,\omega) P(r,\omega) \end{aligned} \qquad \text{(B.3)}$$

where I(r,ω) is the temporal Fourier transform of the instantaneous intensity, P(r, ω) is the temporal Fourier transform of the pressure, and σ(r, ω) is the attenuation cross section of the material. Substituting p(r,t)=ρc u(r,t) into (B.2), and inserting into (B.1), the expression for the ARF becomes

$$F_r(r) = -\rho \frac{2e_z}{T(\rho c)^2} \int_V \int_0^T p(r,t)\, \frac{\mathrm{d}p^*(r,t)}{\mathrm{d}z}\, \mathrm{d}t\, \mathrm{d}V \qquad \text{(B.4)}$$

where the complex conjugate, denoted with an asterisk, is introduced to clearly relate the problem to Plancherel's theorem. Using said theorem with (B.4), the ARF is

$$F_r(r) = -\frac{2e_z}{2\pi T \rho c^2} \int_V \int_{-\infty}^{\infty} P(r,\omega)\, \frac{\mathrm{d}P^*(r,\omega)}{\mathrm{d}z}\, \mathrm{d}\omega\, \mathrm{d}V \qquad \text{(B.5)}$$

And, finally, inserting (B.3), and letting the ARF be uniform over the volume ΔV, the ARF per unit volume can be expressed as

$$\frac{\Delta F_r(r)}{\Delta V} = \frac{e_z}{2\pi T \rho c^2} \int_{-\infty}^{\infty} \sigma_e(r,\omega) |P(r,\omega)|^2\, \mathrm{d}\omega \qquad \text{(B.6)}$$

ACKNOWLEDGMENT

The authors would like to thank Kristin Grendstad, Sigrid Berg, Andreas Åslund, and Rune Hansen for their technical support. The tumor sections were prepared at the Cellular and Molecular Imaging Core Facility (CMIC), Norwegian University of Science and Technology (NTNU). CMIC is funded by the Faculty of Medicine at NTNU and the Central Norway Regional Health Authority.

REFERENCES

[1] R. A. Lake and B. W. S. Robinson, "Immunotherapy and chemotherapy — a practical partnership," *Nat. Rev. Cancer,* Perspective vol. 5, pp. 397-405, May 2005.

[2] Y. Barenholz, "Liposome application: Problems and prospects," *Curr Opin Colloid Interface Sci,* Review vol. 6, no. 1, pp. 66-77, 2001.

[3] V. P. Torchilin, "Recent advances with liposomes as pharmaceutical carriers," *Nat Rev Drug Discov,* 10.1038/nrd1632 vol. 4, no. 2, pp. 145-160, 2005.

[4] E. Sulheim, H. Baghirov, E. von Haartman, A. Bøe, A. K. O. Åslund, Y. Mørch, and C. d. L. Davies, "Cellular uptake and intracellular degradation of poly(alkyl cyanoacrylate) nanoparticles," *J Nanobiotechnology,* journal article vol. 14, no. 1, pp. 1-14, Jan. 2016.

[5] S. R. Croy and G. S. Kwon, "Polymeric micelles for drug delivery," (in eng), *Curr. Pharm. Des.,* vol. 12, no. 36, pp. 4669-84, 2006.

[6] W. H. De Jong and P. J. A. Borm, "Drug delivery and nanoparticles: Applications and hazards," *Int J Nanomedicine,* vol. 3, no. 2, pp. 133-149, Jun. 2008.

[7] P. Zhong, Y. Zhou, and S. Zhu, "Dynamics of bubble oscillation in constrained media and mechanisms of vessel rupture in swl," *Ultrasound Med. Biol.,* vol. 27, no. 1, pp. 119-134, 2001.

[8] M. A. Miller and R. Weissleder, "Imaging the pharmacology of nanomaterials by intravital microscopy: Toward understanding their biological behavior," *Adv. Drug Deliv. Rev.,* no. 113, pp. 61-68, Apr. 2017.

[9] J. Vaage, D. Donovan, P. Uster, and P. Working, "Tumour uptake of doxorubicin in polyethylene glycol-coated liposomes and therapeutic effect against a xenografted human pancreatic carcinoma," *Br. J. Cancer,* vol. 75, no. 4, pp. 482-486, 1997.

[10] C. d. L. Davies, L. M. Lundstrøm, J. Frengen, L. Eikenes, Ø. S. Bruland, O. Kaalhus, M. H. B. Hjelstuen, and C. Brekken, "Radiation Improves the Distribution and Uptake of Liposomal Doxorubicin (Caelyx) in Human Osteosarcoma Xenografts," *Cancer Res.,* vol. 64, no. 2, p. 547, 2004.

[11] Y. H. Bae, "Drug targeting and tumor heterogeneity," *J Control Release,* vol. 133, no. 1, pp. 2-3, Jan. 2009.

[12] L. Eikenes, M. Tari, I. Tufto, O. S. Bruland, and C. de Lange Davies, "Hyaluronidase induces a transcapillary pressure gradient and improves the distribution and uptake of liposomal doxorubicin (Caelyx[trade]) in human osteosarcoma xenografts," *Br. J. Cancer,* vol. 93, no. 1, pp. 81-88, Jul. 2005.

[13] W. T. Phillips, A. Bao, A. J. Brenner, and B. A. Goins, "Image-guided interventional therapy for cancer with radiotherapeutic nanoparticles," *Adv. Drug Deliv. Rev.,* vol. 76, pp. 39-59, Sep. 2014.

[14] V. P. Chauhan, T. Stylianopoulos, J. D. Martin, Z. Popović, O. Chen, W. S. Kamoun, M. G. Bawendi, D. Fukumura, and R. K. Jain, "Normalization of tumour blood vessels improves the delivery of nanomedicines in a size-dependent manner," *Nature nanotechnology,* vol. 7, no. 6, p. 383, 2012.

[15] S. Eggen, M. Afadzi, E. A. Nilssen, S. B. Haugstad, B. Angelsen, and C. d. L. Davies, "Ultrasound Improves the Uptake and Distribution of Liposomal Doxorubicin in Prostate Cancer Xenografts," *Ultrasound Med. Biol.,* vol. 39, no. 7, pp. 1255-1266, Jul. 2013.

[16] V. Frenkel, "Ultrasound mediated delivery of drugs and genes to solid tumors," *Adv. Drug Deliv. Rev.,* vol. 60, no. 10, pp. 1193-1208, Jun. 2008.

[17] E. Hagtvet, T. J. Evjen, D. R. Olsen, S. L. Fossheim, and E. A. Nilssen, "Ultrasound enhanced antitumor activity of liposomal doxorubicin in mice," *J. Drug Target.,* vol. 19, no. 8, pp. 701-708, Sep. 2011.

[18] B. E. O'Neill and K. C. Li, "Augmentation of targeted delivery with pulsed high intensity focused ultrasound," *Int. J. Hyperthermia,* vol. 24, no. 6, pp. 506-520, 2008.

[19] A. Van Wamel, A. Healey, P. C. Sontum, S. Kvåle, N. Bush, J. Bamber, and C. de Lange Davies, "Acoustic Cluster Therapy (ACT) — pre-clinical proof of principle for local drug delivery and enhanced uptake," *J Control Release,* vol. 224, pp. 158-164, 2016.

[20] B. Diener, L. Carrick, and R. S. Berk, "In Vivo Studies with Collagenase from Pseudomonas

aeruginosa," *Infect. Immun.,* vol. 7, no. 2, p. 212, 1973.

[21] S. Kotopoulis, G. Dimcevski, O. H. Gilja, D. Hoem, and M. Postema, "Treatment of human pancreatic cancer using combined ultrasound, microbubbles, and gemcitabine: a clinical case study," (in eng), *Med. Phys.,* vol. 40, no. 7, pp. 072902-9, Jul. 2013.

[22] E. A. Swabb, J. Wei, and P. M. Gullino, "Diffusion and Convection in Normal and Neoplastic Tissues," *Cancer Res.,* vol. 34, no. 10, pp. 2814-2822, 1974.

[23] F. L. Lizzi, R. Muratore, C. X. Deng, J. A. Ketterling, S. K. Alam, S. Mikaelian, and A. Kalisz, "Radiation-force technique to monitor lesions during ultrasonic therapy," (in eng), *Ultrasound Med. Biol.,* vol. 29, no. 11, pp. 1593-605, Nov. 2003.

[24] S. O. Dymling, H. W. Persson, T. G. Hertz, and K. Lindström, "A new ultrasonic method for fluid property measurements," *Ultrasound Med. Biol.,* vol. 17, no. 5, pp. 497-500, Jan. 1991.

[25] J. P. Kilroy, A. L. Klibanov, B. R. Wamhoff, D. K. Bowles, and J. A. Hossack, "Localized in Vivo Model Drug Delivery with Intravascular Ultrasound and Microbubbles," *Ultrasound Med Biol,* vol. 40, no. 10, pp. 2458-2467, 2014.

[26] M. S. Tartis, J. McCallan, A. F. H. Lum, R. LaBell, S. M. Stieger, T. O. Matsunaga, and K. W. Ferrara, "Therapeutic effects of paclitaxel-containing ultrasound contrast agents," *Ultrasound Med. Biol.,* vol. 32, no. 11, pp. 1771-1780, 2006.

[27] M. J. Shortencarier, P. A. Dayton, S. H. Bloch, P. A. Schumann, T. O. Matsunaga, and K. W. Ferrara, "A method for radiation-force localized drug delivery using gas-filled lipospheres," *IEEE Transactions on Ultrasonics, Ferroelectrics, and Frequency Control,* vol. 51, no. 7, pp. 822-831, 2004.

[28] P. A. Dayton, J. S. Allen, and K. W. Ferrara, "The magnitude of radiation force on ultrasound contrast agents," *J. Acoust. Soc. Am.,* vol. 112, no. 5, pp. 2183-2192, 2002.

[29] *Ultrasonics – Hydrophones* IEC 62127-1, 2013.

[30] J. A. Rooney and W. L. Nyborg, "Acoustic Radiation Pressure in a Traveling Plane Wave," *Am J Phys,* vol. 40, no. 12, pp. 1825-1830, 1972.

[31] T. L. Szabo, "Chapter 4 - Attenuation," in *Diagnostic Ultrasound Imaging: Inside Out (Second Edition)*. Boston: Academic Press, 2014, pp. 81-119.

[32] T. Varslot and S.-E. Måsøy, "Forward propagation of acoustic pressure pulses in 3D soft biological tissue," *Model Indent Control,* vol. 27, no. 3, pp. 181-200, 2006.

[33] T. L. Szabo, "Chapter 12 - Nonlinear Acoustics and Imaging," in *Diagnostic Ultrasound Imaging: Inside Out (Second Edition)*. Boston: Academic Press, 2014, pp. 501-563.

[34] K. J. Parker, S. R. Huang, R. M. Leme, F. J. Lee, D. Rubens, and D. Roach, "Elastic and ultrasonic properties of the prostate," in *Proc IEEE Ultrasonm Symp*, 1993, pp. 1035-1038 vol.2.

[35] F. A. Duck, "Chapter 5 - Mechanical Properties of Tissue," in *Physical Properties of Tissues*. London: Academic Press, 1990, pp. 137-165.

[36] Y. A. Ilinskii, G. D. Meegan, E. A. Zabolotskaya, and S. Y. Emelianov, "Gas bubble and solid sphere motion in elastic media in response to acoustic radiation force," *J. Acoust. Soc. Am.,* vol. 117, no. 4, pp. 2338-2346, 2005.

[37] M. Settnes and H. Bruus, "Forces acting on a small particle in an acoustical field in a viscous fluid," *Physical Review E,* vol. 85, no. 1, p. 016327, Jan. 2012.

[38] M. Orescanin, K. S. Toohey, and M. F. Insana, "Material properties from acoustic radiation force step response," *J. Acoust. Soc. Am.,* vol. 125, no. 5, pp. 2928-2936, 2009.

[39] C. W. Wang, M. J. Perez, B. P. Helmke, F. Viola, and M. B. Lawrence, "Integration of Acoustic Radiation Force and Optical Imaging for Blood Plasma Clot Stiffness Measurement," *PLoS One,* vol. 10, no. 6, p. e0128799, 2015.

[40] P. A. Netti, L. T. Baxter, Y. Boucher, R. Skalak, and R. K. Jain, "Time-dependent behavior of interstitial fluid pressure in solid tumors: implications for drug delivery," (in eng), *Cancer Res.,* vol. 55, no. 22, pp. 5451-8, Nov. 1995.

[41] A. Coates, S. Abraham, S. B. Kaye, T. Sowerbutts, C. Frewin, R. M. Fox, and M. H. N. Tattersall, "On the receiving end—patient perception of the side-effects of cancer chemotherapy," *Eur. J. Cancer,* vol. 19, no. 2, pp. 203-208, 1983.

[42] Y. Wang, M. Orescanin, and M. F. Insana, "In vivo measurement of the complex shear modulus of rat mammary tumors using shear wave imaging techniques," in *2010 Annual International Conference of the IEEE Engineering in Medicine and Biology*, 2010, pp. 29-32.

[43] L. E. Shimolina, M. A. Izquierdo, I. López-Duarte, J. A. Bull, M. V. Shirmanova, L. G. Klapshina, E. V. Zagaynova, and M. K. Kuimova, "Imaging tumor microscopic viscosity in vivo using molecular rotors," *Sci. Rep.,* Article vol. 7, p. 41097, Jan. 2017.

[44] M. A. Swartz and M. E. Fleury, "Interstitial Flow and Its Effects in Soft Tissues," *Annu. Rev. Biomed. Eng.,* vol. 9, no. 1, pp. 229-256, Aug. 2007.

[45] A. Zupančič Valant, L. Žiberna, Y. Papaharilaou, A. Anayiotos, and G. C. Georgiou, "The influence of temperature on rheological properties of blood mixtures with different volume expanders—implications in numerical arterial hemodynamics simulations," *Rheologica Acta,* journal article vol. 50, no. 4, pp. 389-402, 2011.

[46] P. Morris, A. Hurrell, A. Shaw, E. Zhang, and P. Beard, "A Fabry–Pérot fiber-optic ultrasonic hydrophone for the simultaneous measurement of temperature and acoustic pressure," *J. Acoust. Soc. Am.,* vol. 125, no. 6, pp. 3611-3622, 2009.

[47] E. Sulheim, J. Kim, A. van Wamel, E. Kim, S. Snipstad, I. Vidic, I. H. Grimstad, M. Widerøe, S. H. Torp, S. Lundgren, D. J. Waxman, and C. de Lange

Davies, "Multi-modal characterization of vasculature and nanoparticle accumulation in five tumor xenograft models," *J. Control. Release,* vol. 279, pp. 292-305, Jun. 2018.

[48] S. M. Stieger, C. F. Caskey, R. H. Adamson, S. Qin, F. R. Curry, E. R. Wisner, and K. W. Ferrara, "Enhancement of vascular permeability with low-frequency contrast-enhanced ultrasound in the chorioallantoic membrane model," (in eng), *Radiology,* vol. 243, no. 1, pp. 112-121, Apr. 2007.

[49] P. A. Dayton, K. E. Morgan, A. L. Klibanov, G. H. Brandenburger, and K. W. Ferrara, "Optical and acoustical observations of the effects of ultrasound on contrast agents," *IEEE Transactions on Ultrasonics, Ferroelectrics, and Frequency Control,* vol. 46, no. 1, pp. 220-232, 1999.

[50] J. Y. Hwang, B. J. Kang, C. Lee, H. H. Kim, J. Park, Q. Zhou, and K. K. Shung, "Non-contact acoustic radiation force impulse microscopy via photoacoustic detection for probing breast cancer cell mechanics," *Biomed Opt Express,* vol. 6, no. 1, pp. 11-22, Jan. 2015.

[51] M. Kaya, C. Toma, J. Wang, M. Grata, H. Fu, F. S. Villanueva, and X. Chen, "Acoustic radiation force for vascular cell therapy: in vitro validation," *Ultrasound Med. Biol.,* vol. 38, no. 11, pp. 1989-1997, Nov. 2012.

[52] D. Thakkar, R. Gupta, K. Monson, and N. Rapoport, "Effect of Ultrasound on the Permeability of Vascular Wall to Nanoemulsion Droplets," *Ultrasound Med. Biol.,* vol. 39, no. 10, pp. 1804-1811, Oct. 2013.

[53] C. H. Heldin, K. Rubin, K. Pietras, and A. Ostman, "High interstitial fluid pressure - an obstacle in cancer therapy," (in eng), *Nat. Rev. Cancer,* vol. 4, no. 10, pp. 806-13, Oct. 2004.

[54] H. A. Hancock, L. H. Smith, J. Cuesta, A. K. Durrani, M. Angstadt, M. L. Palmeri, E. Kimmel, and V. Frenkel, "Investigations into Pulsed High-Intensity Focused Ultrasound–Enhanced Delivery: Preliminary Evidence for a Novel Mechanism," *Ultrasound Med. Biol.,* vol. 35, no. 10, pp. 1722-1736, Oct. 2009.

[55] S. Eggen, S.-M. Fagerland, Ý. Mørch, R. Hansen, K. Søvik, S. Berg, H. Furu, A. D. Bøhn, M. B. Lilledahl, A. Angelsen, B. Angelsen, and C. de Lange Davies, "Ultrasound-enhanced drug delivery in prostate cancer xenografts by nanoparticles stabilizing microbubbles," *J. Control. Release,* vol. 187, pp. 39-49, Aug. 2014.

[56] B. E. O'Neill, H. Vo, M. Angstadt, K. P. C. Li, T. Quinn, and V. Frenkel, "Pulsed High Intensity Focused Ultrasound Mediated Nanoparticle Delivery: Mechanisms and Efficacy in Murine Muscle," *Ultrasound Med. Biol.,* vol. 35, no. 3, pp. 416-424, Mar. 2009.

[57] L. Eikenes, Ø. S. Bruland, C. Brekken, and C. d. L. Davies, "Collagenase Increases the Transcapillary Pressure Gradient and Improves the Uptake and Distribution of Monoclonal Antibodies in Human Osteosarcoma Xenografts," *Cancer Res.,* vol. 64, no. 14, p. 4768, 2004.

[58] R. K. Jain, "Barriers to drug delivery in solid tumors," (in eng), *Sci. Am.,* vol. 271, no. 1, pp. 58-65, Jul. 1994.

[59] M. J. Paszek, N. Zahir, K. R. Johnson, J. N. Lakins, G. I. Rozenberg, A. Gefen, C. A. Reinhart-King, S. S. Margulies, M. Dembo, D. Boettiger, D. A. Hammer, and V. M. Weaver, "Tensional homeostasis and the malignant phenotype," *Cancer Cell,* vol. 8, no. 3, pp. 241-254, Sep. 2005.

[60] Y. Boucher, L. T. Baxter, and R. K. Jain, "Interstitial pressure gradients in tissue-isolated and subcutaneous tumors: implications for therapy," (in eng), *Cancer Res.,* vol. 50, no. 15, pp. 4478-84, Aug. 1990.

[61] H. Lea-Banks, B. Teo, E. Stride, and C. C. Coussios, "The effect of particle density on ultrasound-mediated transport of nanoparticles," *Phys. Med. Biol.,* vol. 61, no. 22, pp. 7906-7919, 2016.

[62] P. A. Dayton, S. Zhao, S. H. Bloch, P. Schumann, K. Penrose, T. O. Matsunaga, R. Zutshi, A. Doinikov, and K. W. Ferrara, "Application of Ultrasound to Selectively Localize Nanodroplets for Targeted Imaging and Therapy," *Mol. Imaging,* vol. 5, no. 3, p. 7290.2006.00019, Jul. 2006.

[63] V. Frenkel, E. Kimmel, and Y. Iger, "Ultrasound-induced intercellular space widening in fish epidermis," *Ultrasound Med. Biol.,* vol. 26, no. 3, pp. 473-480, Mar. 2000.

[64] M. A. Solovchuk, T. W. H. Sheu, W.-L. Lin, I. Kuo, and M. Thiriet, "Simulation study on acoustic streaming and convective cooling in blood vessels during a high-intensity focused ultrasound thermal ablation," *Int J Heat Mass Transfer* vol. 55, no. 4, pp. 1261-1270, Jan. 2012.

[65] E. P. Stride and C. C. Coussios, "Cavitation and contrast: the use of bubbles in ultrasound imaging and therapy," (in eng), *Proc. Inst. Mech. Eng. H,* vol. 224, no. 2, pp. 171-91, 2010.

[66] G. Kong, R. D. Braun, and M. W. Dewhirst, "Characterization of the Effect of Hyperthermia on Nanoparticle Extravasation from Tumor Vasculature," *Cancer Res.,* vol. 61, no. 7, p. 3027, 2001.

[67] S. Wang, I. S. Shin, H. Hancock, B.-s. Jang, H.-s. Kim, S. M. Lee, V. Zderic, V. Frenkel, I. Pastan, C. H. Paik, and M. R. Dreher, "Pulsed high intensity focused ultrasound increases penetration and therapeutic efficacy of monoclonal antibodies in murine xenograft tumors," *J. Control. Release,* vol. 162, no. 1, pp. 218-224, Aug. 2012.

[68] S. B. Barnett, G. R. Ter Haar, M. C. Ziskin, H. D. Rott, F. A. Duck, and K. Maeda, "International recommendations and guidelines for the safe use of diagnostic ultrasound in medicine," (in eng), *Ultrasound Med. Biol.,* vol. 26, no. 3, pp. 355-66, Mar. 2000.

[69] S. Snipstad, S. Berg, Ý. Mørch, A. Bjørkøy, E. Sulheim, R. Hansen, I. Grimstad, A. van Wamel, A. F. Maaland, S. H. Torp, and C. d. L. Davies, "Ultrasound Improves the Delivery and Therapeutic Effect of Nanoparticle-Stabilized Microbubbles in Breast Cancer Xenografts," *Ultrasound Med Biol,* vol. 43, no. 11, pp. 2651-2669, 2017.

TABLE I: PARAMETERS USED EXPERIMENTALLY AND, IN THE SIMULATIONS, AS WELL AS THE MEASURED TRANSDUCER SURFACE POWER AND SIMULATED FOCAL INTENSITY. ACOUSTIC OUTPUT POWER AND DUTY CYCLE WERE LIMITED BY THE SELF-HEATING OF THE TRANSDUCERS

Parameter	**Symbol**	**Excitation frequency (MHz)**	
		5	10
Aperture diameter (mm)	D	29	19
Focus (mm)	Z_{focus}	60	50
-3dB focal area (mm^2)	-	0.31	0.12
3 dB treated area (mm^2)	-	3.24	1.08
Pulse duration (µs)	T_p	1.0	0.5
Pulse repetition period (ms)	T_R	0.167	0.015
Pulse repetition frequency (kHz)	$PRF=\frac{1}{T_R}$	6	66
Duty cycle (%)	$DC=\frac{T_P}{T_R}100$	0.6	3.3
Total time (s)	$T_{on}=\frac{DC}{100}T_{tot}$	2.4	13.2
Total scanning time for at given location (s)	T_{tot}	400	400
Transducer surface pressure* (kPa)	-	133	206
Peak transducer surface power* (W)	-	4	4.2
Average transducer surface power* (mW)	-	24	139
Peak focal intensity** (W/cm^2)	I_{SATP}	337	234
Average focal intensity ** (W/cm^2)	I_{SATA}	2.02	7.72
Mechanical index**	MI	1.36	1.01

*) Measurement results, **) Simulation results, I_{SATP} – spatial average temporal peak intensity, I_{SATA} – spatial average temporal average intensity

TABLE II: SIMULATED DISPLACEMENT OF NP IN BLOOD AND ECM DUE TO ARF

US exposure			**ARF**	**Displacement of NP in blood**	**Displacement of NP in ECM**	
					Direct effect on NP	Acoustic streaming on NP
f (MHz)	DC (%)	I_{SATP} (W/cm^2)	X10^6 (Nm^2)	µm	µm	µm
5	0.6	337	0.7	0.25	0.008-0.26	0.012-12
10	3.3	234	2	2.3	0.07-2.2	0.2-200

A range of displacement are indicated as a range of values for viscosity and hydraulic conductivity are used. DC is the duty cycle

TABLE III: HYDROPHONE MEASUREMENT PARAMETERS USED TO ESITMATE SURFACE PRESSURE

Parameter	**Symbol**	**Excitation frequency (MHz)**	
		5	10
Characteristic impedance (MRayl)	Z	1.5	1.5
Low voltage, peak-to-peak (V)	V_{pp}^{L}	15	11
High voltage, peak-to-peak (V)	V_{pp}^{H}	160	210
Near-field measurement grid depth (mm)	Z_0	1.0	1.0
Far-field measurement depth (mm)	Z_1	55	45
Far-field measurement grid resolution (mm)	(Δx, Δy)	(0.1, 0.1)	(0.1, 0.1)
Far-field measurement grid point	(I+1, J+1)	(61, 61)	(41, 41)
Far-field measurement grid size (mm)	(IΔx, JΔ)	(3.0, 3.0)	(2.0, 2.0)

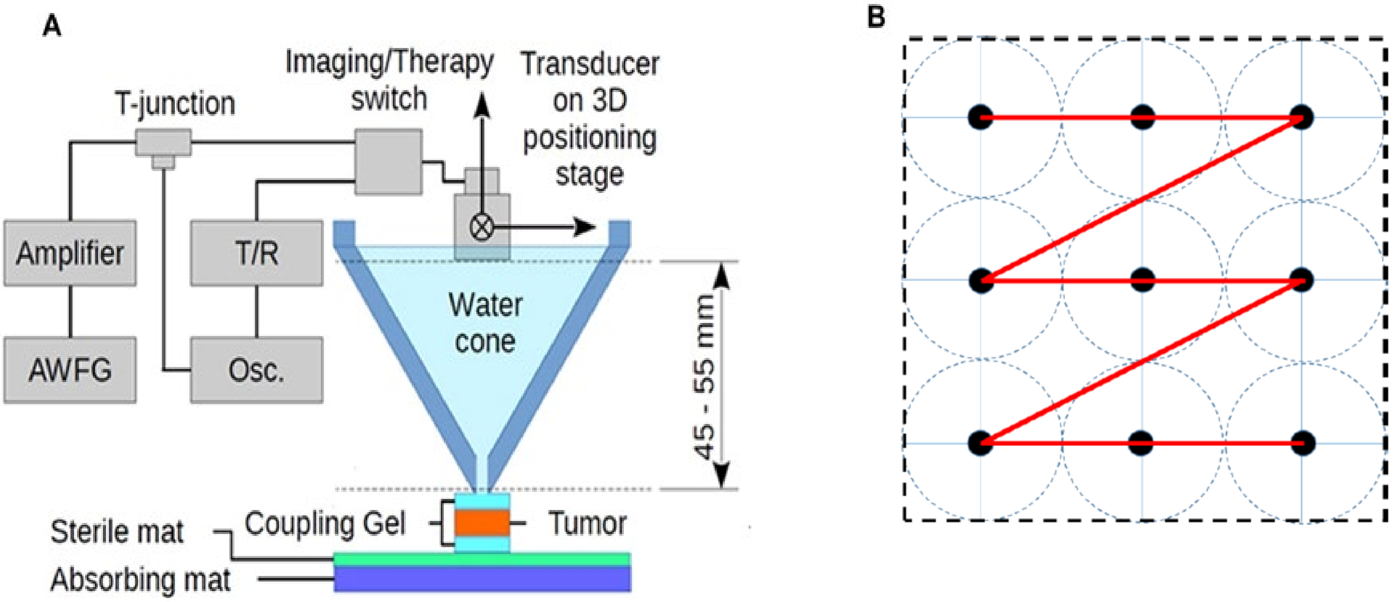

Fig. 1: Schematic illustration of the experimental setup showing the oscilloscope (Osc), arbitrary wave form generator (AWFG), amplifier and the pulse/receiver (T/R) used for the US exposure of the tumors (A). The imaging/therapy switch was operated by manually changing the connections to the transducer. The US beam was focused onto the tumor on the leg of the mice which was placed on an absorbing mat. The water cone was replaced with a plastic bag in the 5 MHz experiment. B) shows the scanning pattern of the stepping motor used to move the transducer during US exposure of the tumors. The distance between each point in the pattern corresponds to the -3dB focal width of the transducer. The dashed square corresponds to the treated xy area.

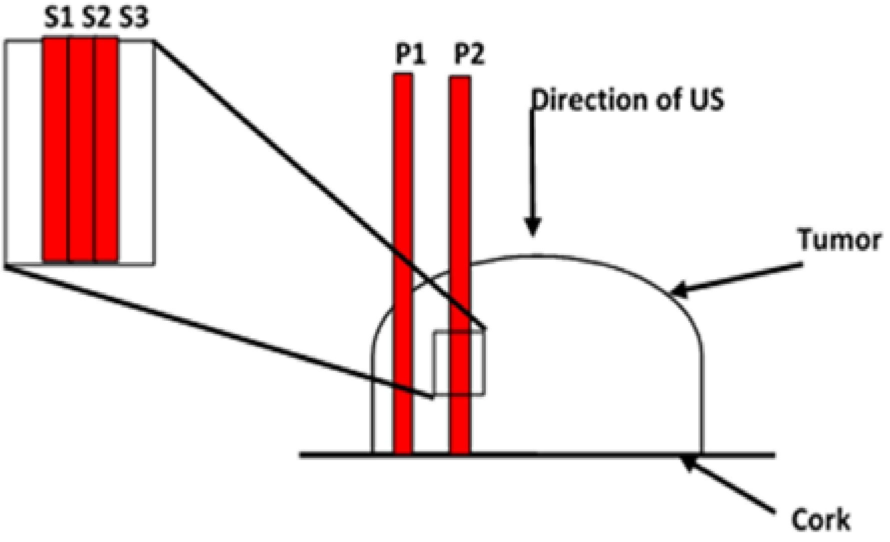

Fig. 2: Schematic illustration of tumor sectioning for CLSM analysis. After removing 500 µm from the edge, the tumor was cut into 25 µm thick frozen sections (S1 – S3). Three sections made up a position (P) with 200 µm distance between each position. The tumor was sectioned until 6 mm or 8 mm depending on the size of the tumor

.

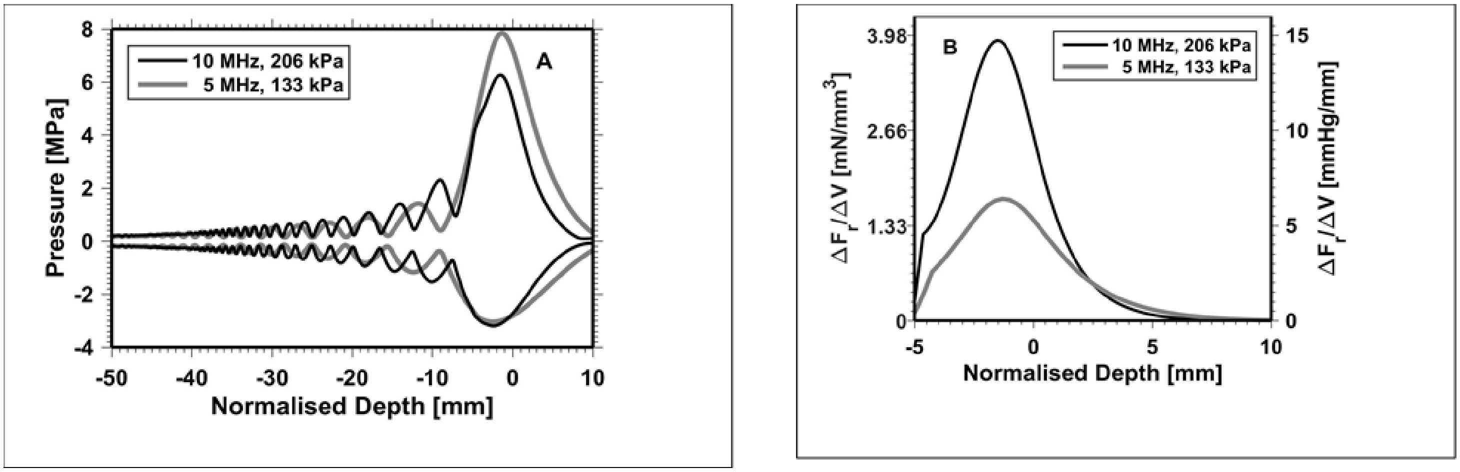

Fig. 3: Peak positive and negative pressures (A) and ARF (B) as a function of normalized depth for both 5 and 10 MHz transducer with power law exponent b = 1.3. The depth coordinate is normalized ($Z_{norm} = Z - Z_{focus}$) so the focus of each transducer is at Z_{norm} = 0 mm. Z_{focus} for 5 and 10 MHz is 60 and 50 mm respectively.

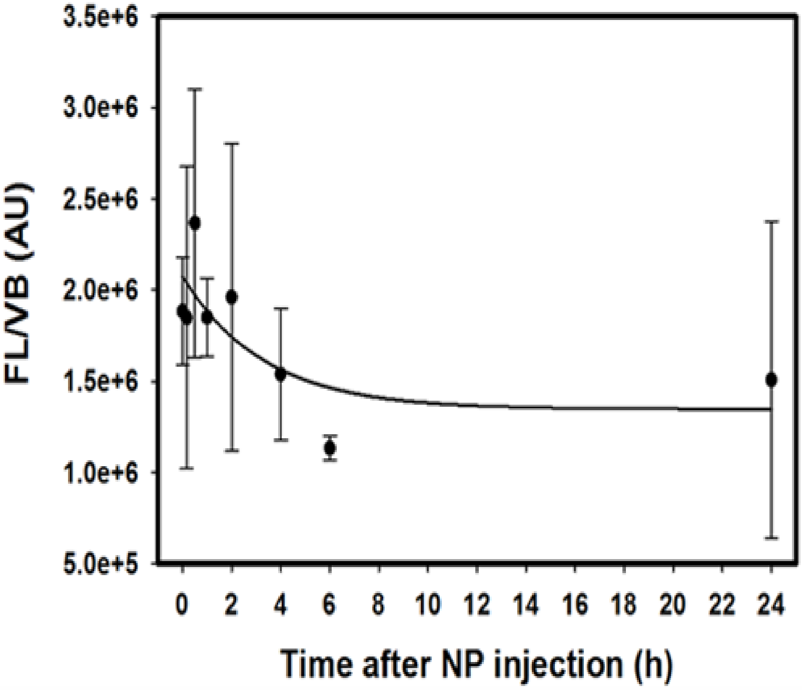

Fig. 4: Circulation time of NPs. The ratio between the fluorescent intensity from NPs and volume of blood (FL/VB) in arbitrary (AU) units as a function of time after injection. Each data point is the mean of n=4 mice and the standard bar=SD. Time point 0 is before NP injection. A biexponential function was fitted to the data.

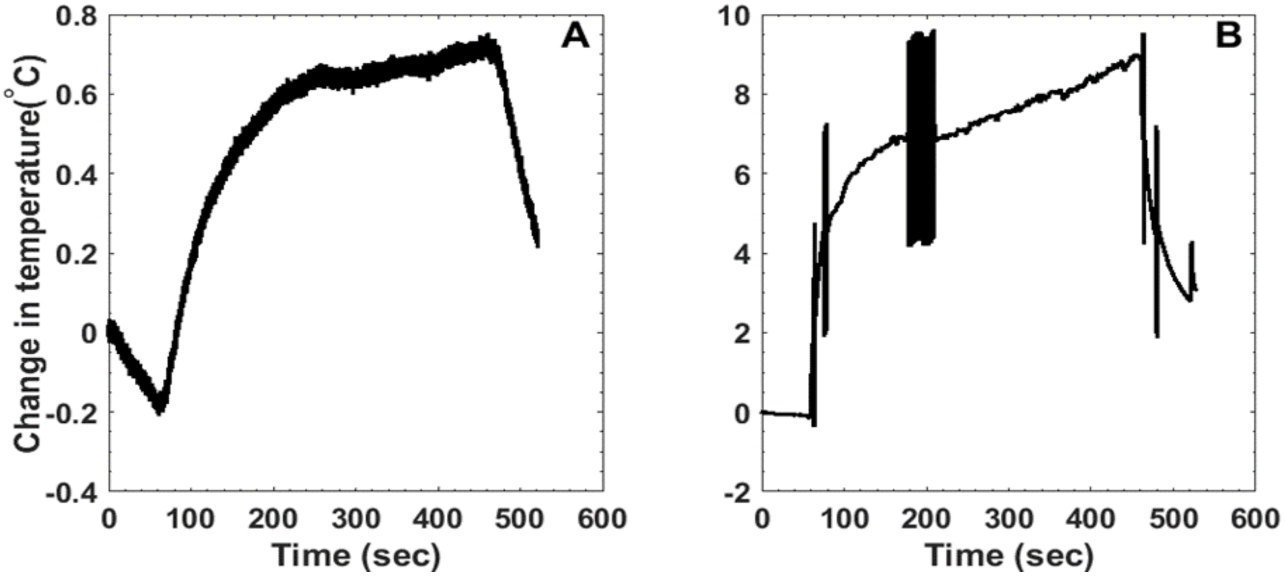

Fig. 5:Temperature increase as a function of time for the 5 MHz (A) and the 10 MHz transducer (B). US was given for 400 s from time 60 s

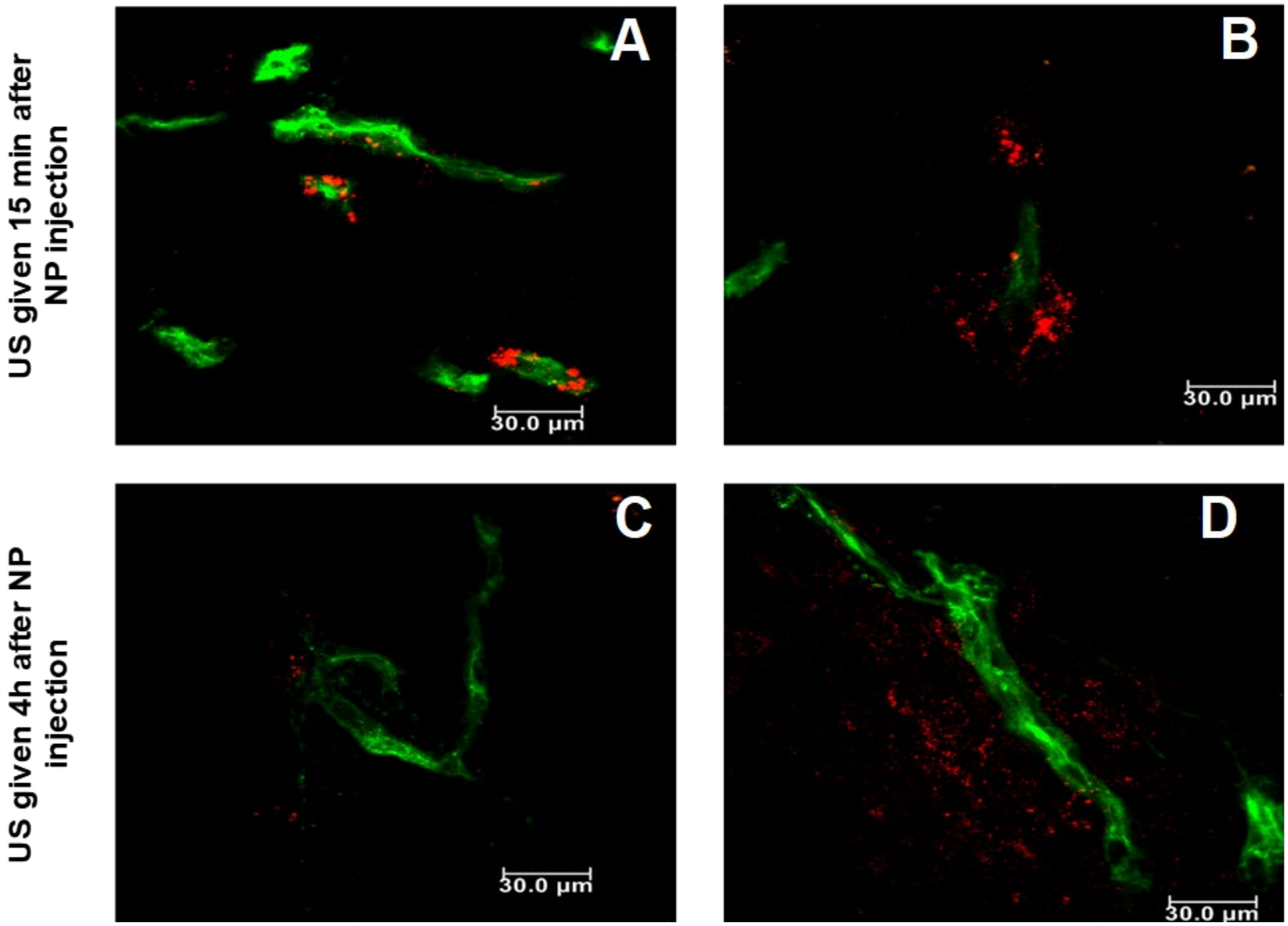

Fig. 6: Distribution of NPs in tumor tissue. CLSM images showing NPs in red and BVs in green, 15 min and 4 h after injection of NPs. Tumors were exposed to no US (A and C), and 10 MHz US (B and D). Scale bar = 30 µm.

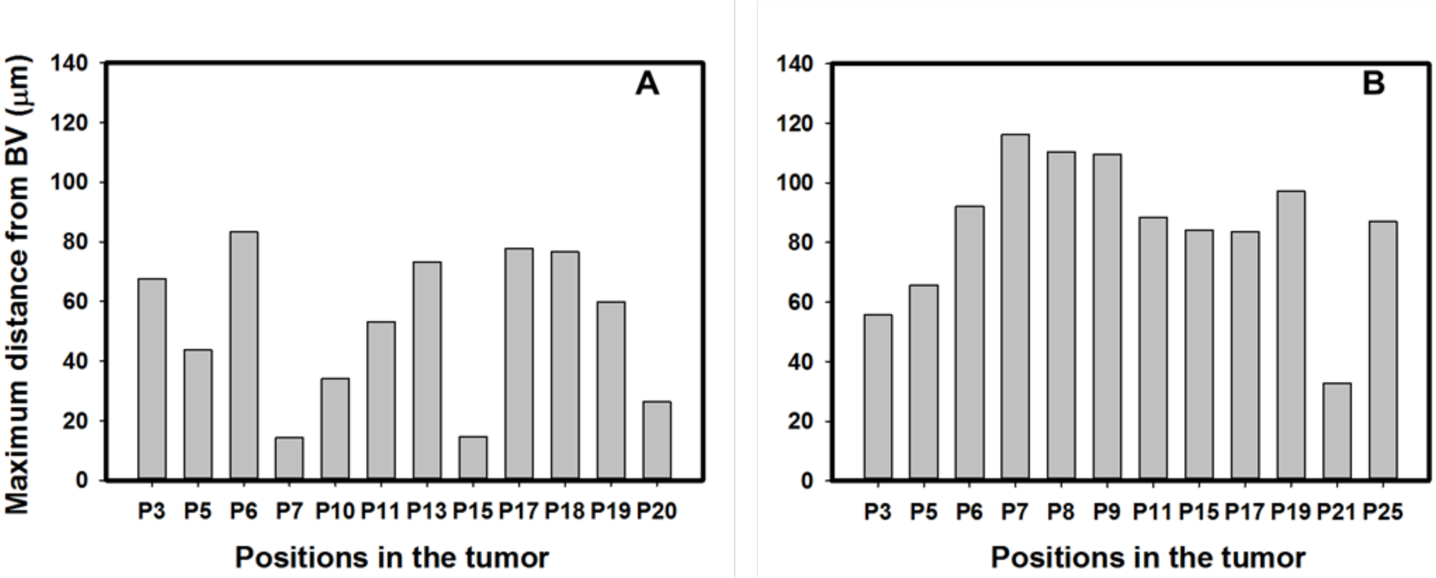

Fig. 7: Maximum distance travelled by the NPs as a function of position throughout the tumor in the control (A) and 10 MHz US (B) 15 min after NP injection.

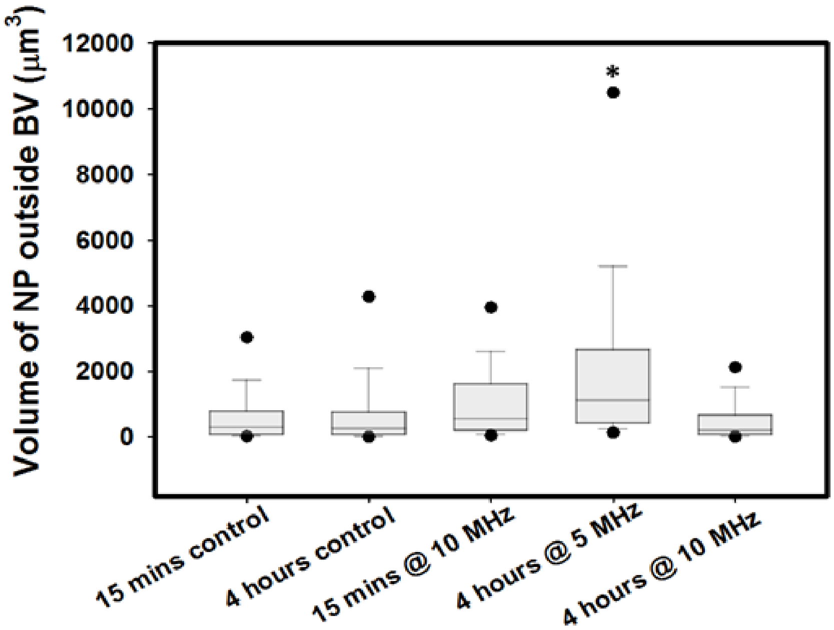

Fig. 8: Volume of NPs outside BVs presented as box plot. US was given 15 min or 4 h after NP injection. Median NP volume per image are presented solid lines, 5th and 95th percentiles are indicated by circles (●) and * indicates $p < 0.05$ (treated groups compared to control group). The plots are based on data from 86 – 394 stacks analyzed per treatment group with n = 6 mice in 15 min control, n = 9 for 4 h control, n = 3 for 10 MHz 15 min, n = 2 for 5 MHz 4h, n=5 for 10 MHz 4 h.

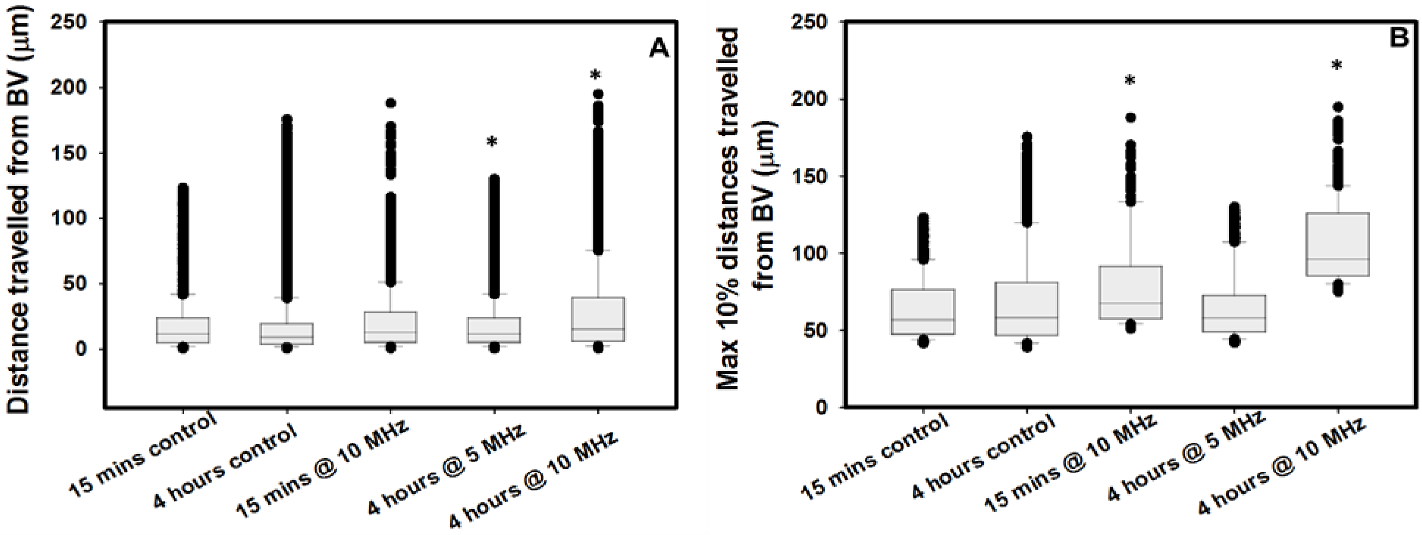

Fig. 9: Distances travelled by NPs from the nearest BV into tumor tissues, presented in box plot. The median distances are presented as solid lines. Outliers are indicated by circles (●) and * indicates $p < 0.05$ (treated groups compared with control group). A shows the distance travelled by all NPs whereas B shows the 10% longest distances travelled by the NPs from the nearest BV. The box plots are based on data from 86 – 394 stacks analyzed per treatment group with n = 6 in 15 min control, n = 9 for 4 h control, n = 3 for 10MHz 15 min, n = 2 for 5 MHz 4h, n=5 for 10 MHz 4 h.

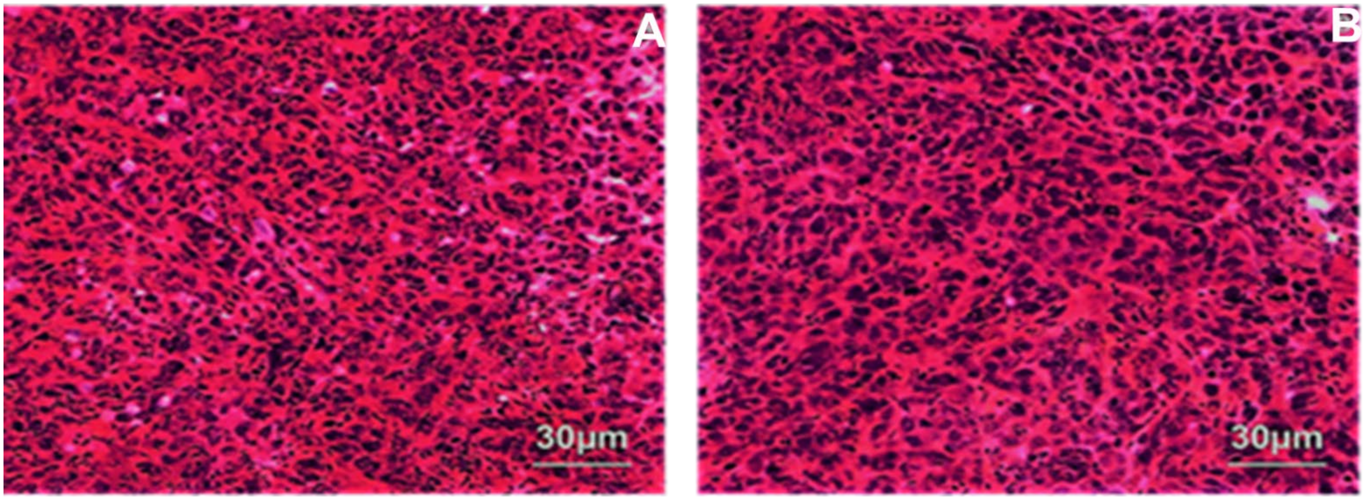

Fig. 10: Histological images (HES staining) from unexposed (A) and tumors exposed to 10 MHz US and 3.3% duty cycle (B). Scale bar = 30 µm.